

# Dynamic Calibration Enables High-Accuracy Charge Measurements on Individual Ions for Charge Detection Mass Spectrometry

Aaron R. Todd and Martin F. Jarrold\*


 Cite This: *J. Am. Soc. Mass Spectrom.* 2020, 31, 1241–1248

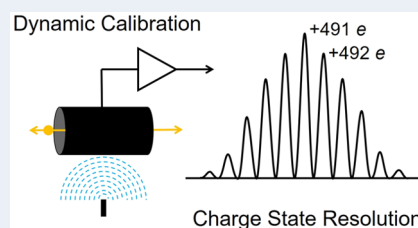

Read Online

ACCESS |

 Metrics & More

 Article Recommendations

**ABSTRACT:** Charge detection mass spectrometry (CDMS) depends on the measurement of the charge induced on a cylinder by individual ions by means of a charge-sensitive amplifier. For high-accuracy charge measurements, the detection cylinder is embedded in an electrostatic linear ion trap (ELIT), and the ions oscillate back and forth through the cylinder so that multiple measurements are made. To assign the charge state with a low error rate, the charge of each ion must be determined with an uncertainty (root-mean-square deviation) of around 0.2 elementary charges. We show here that high-accuracy charge measurements can be achieved for large ions by dynamic calibration of the charge measurement using an internal standard. The internal standard is generated by irradiating the detection cylinder, by means of a small antenna, with a radiofrequency signal. Using this approach, we have obtained a relative charge uncertainty of around  $5 \times 10^{-4}$ , allowing charge-state resolution to be achieved for single ions with up to 500 charges. In another application of this approach, the detection cylinder is irradiated with a signal that counteracts the transients generated when the potentials on the ELIT end-caps are switched to trapping mode. Using this approach, the dead time after switching (during which the signal cannot be analyzed) has been reduced by more than an order of magnitude. With charge-state resolution for ions with up to 500 charges, we were able to calibrate the charges precisely. The results show that the response of the charge-sensitive amplifier with dynamic calibration is linear to within a small fraction of an elementary charge.



## INTRODUCTION

Charge detection mass spectrometry (CDMS) has emerged as an important approach to determining accurate masses for objects beyond the range of conventional mass spectrometry.<sup>1–30</sup> CDMS is a single-particle approach where the masses of individual ions are determined from measurements of each ion's  $m/z$  ratio and charge. The ions pass through a conducting cylinder, and the charge induced on the cylinder is detected by a charge-sensitive amplifier. If the cylinder is long enough the induced charge equals the charge on the ion.<sup>31,32</sup> For high-precision measurements the cylinder is embedded in an electrostatic linear ion trap, and the ion oscillates back and forth through the detector.<sup>3</sup> The resulting time domain signal is analyzed by fast Fourier transforms (FFT).<sup>11,33</sup> The oscillation frequency yields the ion's  $m/z$ , and the FFT magnitude provides the charge. The resolving power of CDMS depends on the uncertainties in the  $m/z$  and charge measurements. Historically, the uncertainty in the charge measurement limited the mass-resolving power.

When the uncertainty in the charge measurement is low, charge states in the charge spectrum are sufficiently resolved that the charge can be quantized, i.e., each ion can be assigned a charge equal to the nearest integer value. In principle, quantizing the charge removes the uncertainty in the charge measurement. However, there is still the possibility of assigning the ion to the wrong charge state. This problem is illustrated in Figure 1. The dashed black line shows a Gaussian distribution

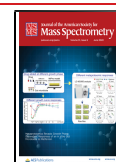
with a root-mean-square deviation (RMSD) of 0.1  $e$  (elementary charges). The  $x$ -axis is the residual charge (the measured charge minus the integer charge), and it extends from a charge of  $-0.5 e$  to  $+0.5 e$ , which is the charge window associated with a charge state. In this case, the distribution (the dashed line) falls almost entirely within the  $-0.5 e$  to  $+0.5 e$  window, and the charge state can be assigned with a very low error rate. However, obtaining a charge RMSD of 0.1  $e$  is difficult, and it is beyond the minimum needed to resolve the charge states. For example, consider the situation where the charge RMSD is 0.25  $e$  (the red line in Figure 1). Notice that the distribution extends to charges smaller than  $-0.5 e$  and larger than  $+0.5 e$ . Thus, some of the ions with this charge state will be assigned to lower and higher charge states. It follows that some of the ions associated with lower and higher charge states will be assigned to this charge state. The green line shows the tail of the distribution from the lower charge state, and the yellow line shows the tail from the higher charge state. In this case, 95.5% of the ions are assigned to the correct

Received: March 5, 2020

Revised: April 20, 2020

Accepted: April 21, 2020

Published: April 30, 2020



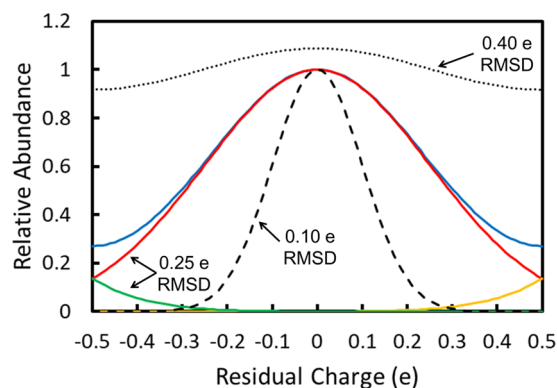


**Figure 1.** Plot showing the consequences of overlapping charge distributions in the charge spectrum. The dashed black line shows a Gaussian distribution of residual charges (measured charges minus the integer charge) for an uncertainty (RMSD) of  $0.1 e$  (elementary charges). In this case, the distribution is narrow and falls almost entirely within the  $-0.5 e$  to  $+0.5 e$  window associated with the integer charge. With a RMSD of  $0.25 e$  (red line) the Gaussian distribution spills out of the  $-0.5 e$  to  $+0.5 e$  window, and the tails from the charge states at  $-1 e$  and  $+1 e$  fall into the  $-0.5 e$  to  $+0.5 e$  window (green and yellow lines). Adding these tails to the Gaussian distribution centered on  $0 e$  (red line) gives the blue line, which represents the measured charge distribution for a RMSD of  $0.25 e$ . Despite some overlap, the charge states are still well-resolved with this RMSD. The dotted black line shows the measured charge distribution for a RMSD of  $0.40 e$ . With this RMSD, the charge-state resolution is essentially lost.

charge state, while 2.25% of the ions are mis-assigned to a lower charge state, and the same percentage are mis-assigned to a higher charge state. It is evident from Figure 1 that most of the mis-assigned ions are close to the  $-0.5 e$  and  $+0.5 e$  dividing lines between the charge states. By discarding ions close to the dividing lines, the number of mis-assigned ions can be dramatically reduced. Thus, if ions outside the range of  $-0.25 e$  to  $+0.25 e$  are discarded, the error rate can be reduced by more than an order of magnitude.

The blue line in Figure 1 was obtained by adding the Gaussian centered on a residual charge of  $0 e$  (the red line) to the tails from Gaussians centered on residual charges of  $-1 e$  and  $+1 e$  (the green and yellow lines). The blue line represents the charge spectrum that would be measured for a RMSD of  $0.25 e$ . While the charge states overlap somewhat, they are still well-resolved. Finally, the dotted black line in Figure 1 shows the distribution that would be measured with a RMSD of  $0.4 e$ . The charge-state resolution is almost completely lost. In this case, assigning the ions to integer charge states actually reduces the charge accuracy.

The charge RMSD is proportional to  $t^{-1/2}$ , where  $t$  is the trapping time. Some time ago we showed that with a 3 s trapping time the charge for pyruvate kinase (PK) tetramer ( $PK_4$ ), octamer ( $PK_4$ )<sub>2</sub>, dodecamer ( $PK_4$ )<sub>3</sub>, and hexadecamer ( $PK_4$ )<sub>4</sub> could be measured with a RMSD of around  $0.2 e$ .<sup>34</sup> In subsequent work, we attempted to resolve charge states for hepatitis B virus (HBV) capsids and brome mosaic virus (BMV), but we were not successful, even when using a trapping time of 30 s. The HBV and BMV ions have much higher masses and are more highly charged than the PK oligomers. The uncertainty in the charge is not thought to depend on the charge; however, the much higher charge on the HBV and BMV ions could contribute to the difficulty of

resolving the charge states. In addition, HBV and BMV have much larger  $m/z$ 's than the PK oligomers. A larger  $m/z$  leads to a lower oscillation frequency and a lower oscillation frequency leads to more  $1/f$  noise, which will in turn increase the uncertainty in the charge measurement. There are probably other factors such as small variations in amplifier gain (see below) that also contributed to our inability to obtain charge-state resolution for HBV and BMV.

Since the early work described above, we have made a number of significant technical improvements. The design for the ELIT has been optimized to reduce the uncertainty in the charge measurement,<sup>34</sup> and we have developed a new custom design for the charge-sensitive amplifier with reduced  $1/f$  noise.<sup>35</sup> However, these changes alone were insufficient to achieve charge-state resolution for highly charged ions. In this manuscript, we describe another technical improvement that we call dynamic calibration. With dynamic calibration, the charge-sensitive amplifier is calibrated during the measurement. A small antenna is placed in the outer casing of the ELIT. A reference radio frequency (RF) signal is applied to the antenna. The signals from the RF reference and oscillating ions are picked up by the detection cylinder and analyzed by a fast Fourier transform. The amplitude of the reference signal is used to correct for small variations in the gain of the charge-sensitive amplifier. Using this approach, we have achieved charge-state resolution for P22 procapsid ions with 500 charges. This dramatically extends the mass range where perfect charge accuracy can be obtained with CDMS.

To trap an ion in an electrostatic ion trap, it is necessary to change the potential(s) on one or more of the trap electrodes from values where ions are allowed to enter and exit the trap to values where ions inside the trap are trapped. The switching of the potentials from transmission mode to trapping mode induces transients on the other components of the trap. In particular, the transient on the detection electrode can be large enough to require a settling time or dead time during which the data cannot be analyzed. The transients are particularly large when there is a direct line of sight between the electrodes that switch potentials and the detection electrodes. The Gen6 ELIT used here does not suffer from that defect. However, even when there is not a direct line of sight there are still significant transients, which can saturate the output of the charge-sensitive amplifier. Over time, the transients caused the charge-sensitive amplifier used in this work to latch up, and in order to reset the amplifier, it was necessary to cycle the temperature of its cryogenically cooled input JFET to room temperature and back to low temperature. (The input JFET is cooled to minimize noise.) We found that the transients could be substantially reduced by irradiating the detection cylinder with a signal that almost completely canceled-out the transients. This solved the latch-up problem and significantly reduced the dead time so that we could start analyzing the time-domain data 0.3 ms after the trap was closed.

## CDMS INSTRUMENT AND EXPERIMENTAL METHODS

The studies reported here were performed on our second generation CDMS instrument that incorporates an electrostatic linear ion trap (ELIT) with improved  $m/z$ -resolving power and charge accuracy. Ions are generated by nanoelectrospray (Advion Biosciences, Triversa NanoMate). They enter the instrument through a heated metal capillary (0.762 mm ID, 10 cm long) and pass through several regions of differential

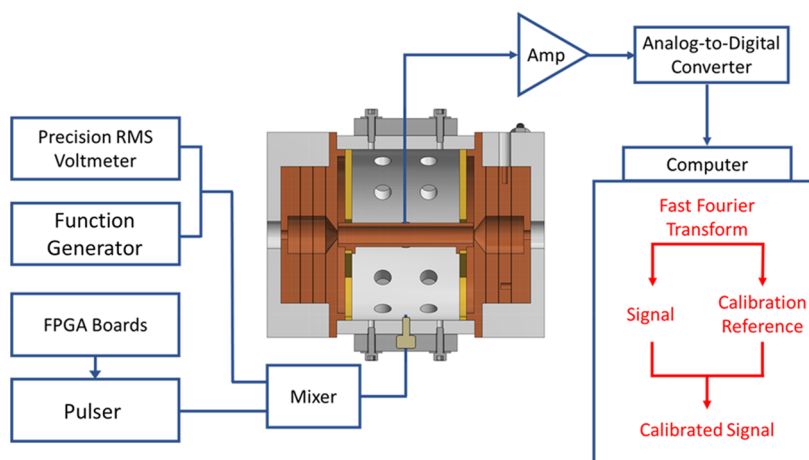


**Figure 2.** Schematic diagram showing the electrostatic linear ion trap with an antenna inserted through the outer (grounded) shield. The antenna radiates the calibration and compensation signals, which are picked-up, along with the ion signals, by the detection cylinder and charge-sensitive amplifier. The signal from the charge-sensitive amplifier is digitized and then sent to a computer for analysis by a Fortran program, which separates the calibration reference signal from the ion signal to generate a calibrated ion signal.

pumping before reaching the ELIT. The first differentially pumped region contains a FUNPET (an ion funnel-ion carpet hybrid) designed to optimize ion transmission over a broad mass range.<sup>36</sup> The second differentially pumped region contains an RF hexapole with a DC offset that sets the ion energy. The hexapole is followed by a segmented RF quadrupole. Ions that exit the quadrupole are focused into a dual hemispherical deflection energy analyzer (HDA), which selects a narrow band of ion kinetic energies. Ions that are transmitted by the HDA enter the fifth differentially pumped region that houses the ELIT. The pressure in this region is around  $10^{-9}$  mbar.

A schematic diagram of the ELIT is shown in Figure 2. The ELIT consists of two end-caps that can be switched between transmission and reflection mode. With both end-caps in reflection mode, ions oscillate back and forth through a metal cylinder located between the end-caps. When ions are in the cylinder, they induce a charge that is detected by the charge-sensitive amplifier. The voltage output from the charge-sensitive amplifier is amplified, digitized, and sent to a computer. The time domain signals are analyzed in real time by a Fortran program which uses a Gaussian window function and fast Fourier transforms to determine the  $m/z$  and charge of the trapped ions.<sup>11,33</sup> Trapping events are discarded if the ions are not trapped for the full trapping time or if a statistical analysis shows that the  $m/z$  or charge values are not stable. Unusual shifts or excursions of the  $m/z$  or charge can arise from mass or charge loss or from multiple ions with similar  $m/z$  values oscillating almost in phase.

The charge-sensitive amplifier employed in this work<sup>35</sup> is based on the approach of Bertuccio and co-workers,<sup>37</sup> where the feedback resistor is removed, and the input JFET is biased by its gate leakage current. Cryogenically cooling the input JFET significantly reduces the noise. However, the gain varies inversely with temperature. To ameliorate this problem, we temperature regulate the cooled JFET so that the temperature variations are less than 0.1 K.<sup>35</sup>

The antenna that is used to irradiate the detection cylinder with the calibration and compensation signals penetrates through the grounded shield of the ELIT. It is located at the bottom of the ELIT in Figure 2. This location allows the calibration and compensation signals to be picked-up on the

detection cylinder and measured by the charge-sensitive amplifier in the same fashion as the signal from an oscillating ion. The signal applied to the antenna is generated in a mixer that combines the reference signal and the signals that compensate for the transients caused by switching the end-caps to trapping mode. The RF reference signal is derived from a function generator (Agilent Technologies, 33220A). A frequency of 128693 Hz was employed. This frequency corresponds to an  $m/z$  of 161.8 Da, which is below the  $m/z$  cutoff of the RF quadrupole, so ions cannot interfere with the calibration signal. The long-term stability of the reference signal is monitored by a high-precision ( $6^{1/2}$  Digit) RMS voltmeter (Keithley 2000 Multimeter). To counteract the transients caused by the switching of the end-caps to trapping mode, the trigger signal is sent to a home-built pulser similar in design to the ones used to switch the potentials on the end-caps. The signals from the pulsers are combined with the reference signal in a mixer, and the resulting signal is applied to the antenna. The amplitude and rise and fall times of the pulses output by the pulsers are adjusted to optimize the transient compensation.

The amplitude of the RF reference signal is simultaneously determined by the same program that analyzes the time domain signals to obtain the oscillation frequency ( $m/z$ ) and amplitude (charge) for trapped ions. The measured amplitudes of the reference signal are averaged over a predetermined number of trapping events, and then, the average amplitude is used to correct the measured charge. In the measurements reported here, the averaging was performed over the current measurement and preceding measurements. The results obtained from averaging over measurements before and after the current measurement were almost identical. This is consistent with the idea that variations in the amplifier gain occur on a longer time scale than the averaging of the reference signal.

CDMS measurements were performed for ubiquitin, pyruvate kinase (PK), and hepatitis B virus (HBV) capsids assembled from truncated core protein Cp149, brome mosaic virus (BMV) virions, and bacteriophage P22 procapsids. Ubiquitin (Sigma-Aldrich) was prepared in a 49/49/2 volume mix of methanol, water, and acetic acid at 0.05  $\mu\text{g}/\text{mL}$ . PK (Sigma-Aldrich) was prepared at 2.0  $\mu\text{g}/\text{mL}$  in 100 mM

ammonium acetate (Sigma-Aldrich,  $\geq 99.99\%$ ) and purified by size-exclusion chromatography (SEC) (Micro Bio-Spin P-6 Gel Columns, BIO-RAD). The HBV sample (provided by Prof Zlotnick, Indiana University) was assembled at 2 mg/mL in 300 mM sodium chloride, transferred into 100 mM ammonium acetate by SEC, and diluted to 0.5 mg/mL before being electrosprayed. The BMV (provided by Prof Dragnea, Indiana University) was transferred into 100 mM ammonium acetate by SEC before being electrosprayed. P22 procapsids (provided by Prof Dragnea, Indiana University) were transferred into 100 mM ammonium acetate before being electrosprayed. The masses determined by CDMS were in the expected ranges (PK tetramer, 234 kDa; HBV  $T = 4$  capsids 4.04 MDa; BMV virions 4.70 MDa; and P22 procapsids 24.4 MDa).

## RESULTS AND DISCUSSION

### Compensation of Transients Minimizes Dead Time.

Figure 3a shows a typical output from the analog to digital

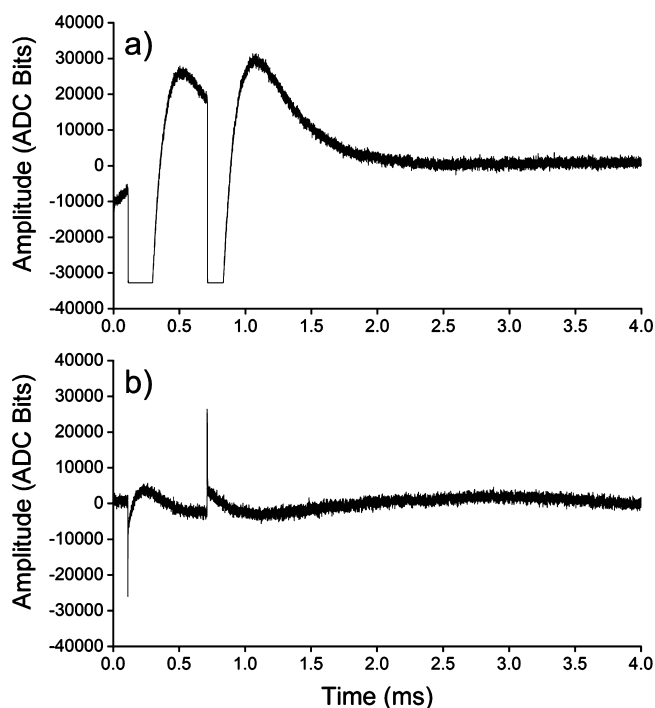


**Figure 3.** Results showing the compensation of the transients caused by end-cap switching. (a) Shows the output from the analog to digital converter following the switching of the ELIT end-caps at 0.1 ms (back end-cap) and 0.7 ms (front end-cap). The large negative going transients eventually caused the charge-sensitive amplifier to latch up. (b) Shows the output with compensation.

converter (ADC) plotted against time for a short time period spanning immediately before and immediately after switching the end-caps to trapping mode. The first minimum at around 0.2 ms results from the switching of the back end-cap at around 0.1 ms, and the second minimum at around 0.8 ms corresponds to the switching of the front end-cap at around 0.7 ms. The ADC employed here has a resolution of 16 bits, with values ranging from  $-32768$  to  $+32768$ . It is evident from Figure 3a that switching the end-caps generates a transient that drives the input to the ADC below the acceptable range, driving the output to saturate at the most negative value. As noted above, we found that operating in this mode eventually

caused the charge-sensitive amplifier to latch-up, and in order to reset the amplifier, it was necessary to temperature cycle the cryogenically cooled input JFET to room temperature and back to low temperature, wasting a lot of time.

The transient compensation approach was devised to shorten the settling time and to stop the charge-sensitive amplifier from latching up. Figure 3b shows a typical output from the ADC with the transient compensation implemented. While transients are still evident, their amplitudes and widths are substantially reduced. With further refinement of the compensation pulse width and rise and fall times, we expect that the transient could be reduced even further. However, with the reduction shown in Figure 3b, the charge-sensitive amplifier no longer latched up. Without compensation (Figure 3a), it takes just over a millisecond for the baseline to recover from the transients. However, it takes considerably longer (4–5 ms after the second switching event) for the amplifier gain to recover so that the amplitude of the reference signal is  $>99.9\%$  of the expected value. With compensation, the signal amplitude is completely recovered 0.3 ms after the second switching event. Thus, the dead time is reduced by more than an order of magnitude.

**Dynamic Calibration Enables High-Accuracy Charge Measurements.** Dynamic calibration was implemented to correct for drift in the gain of the charge-sensitive amplifier over time. Figure 4 shows a plot of the measured calibration

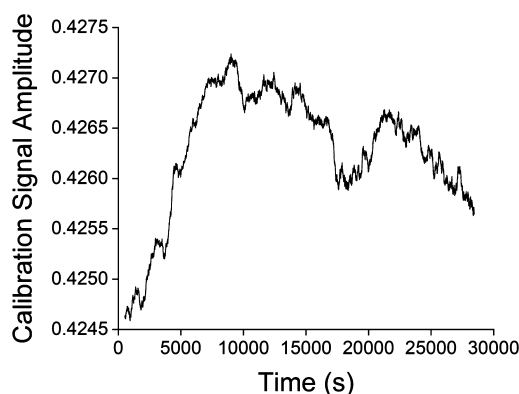


**Figure 4.** The measured calibration signal amplitude plotted as a function of time over an 8 h period. During this time period, the amplitude of the calibration signal (from the RMS voltmeter) did not change significantly, so changes in the measured amplitude are entirely due to variations in the amplifier gain.

signal amplitude during the course of a day (8 h). Note that the amplitude of the calibration signal (as monitored by the RMS voltmeter) did not change significantly during this time period and changes in the measured amplitude are entirely due to variations in the amplifier gain. The variation in the amplitude over this time period is only around 0.5%. However, this would mean that the uncertainty in the charge measurement for an ion with a charge of  $100 e$  is  $>0.5 e$ , which is unacceptably large and rules out the prospect of obtaining charge-state resolution except for ions with a very low charge. Dynamic calibration corrects for both short-term and long-term drifts in the gain of the amplifier that would make accurate charge measurements impossible.

**Charge-State Resolution for Hepatitis B Virus Capsids and Bacteriophage P22 Procapsids.** The icosahedral  $T = 4$  capsid of hepatitis B virus (HBV) assembled from truncated

capsid protein (Cp149) has a diameter of around 36 nm and a mass of around 4.04 MDa.<sup>38,39</sup> CDMS measurements were performed using a trapping time of 1.5 s. Figure 5a shows the

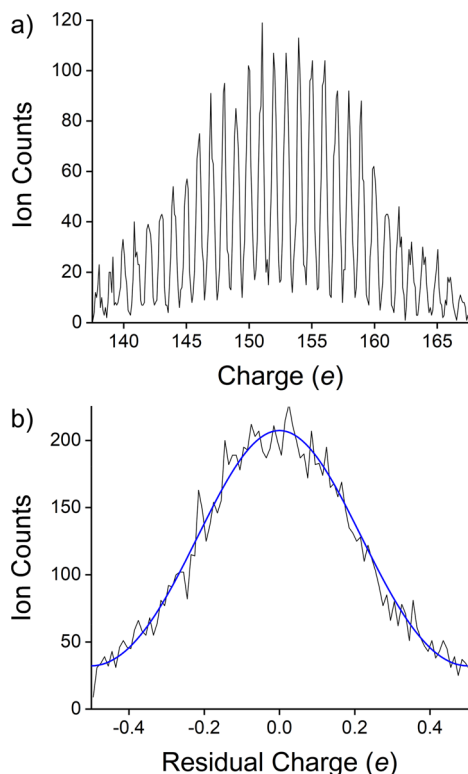


**Figure 5.** Charge-state resolution for the HBV  $T = 4$  capsid. (a) The charge histogram generated using  $0.1 e$  bins. (b) The residual charge histogram plotted with a bin size of  $0.01 e$ . The residual charge is the measured charge minus the integer charge. The blue line was obtained by fitting a Gaussian function to the residual charge histogram. The Gaussian function was obtained by adding a Gaussian centered on a residual charge of  $0 e$  to the tails of identical Gaussians located at residual charges of  $-1.0 e$  and  $+1.0 e$ . The RMSDs of the component Gaussians were adjusted in unison to give the best fit to the histogram.

charge histogram generated using  $0.1 e$  bins for the  $T = 4$  HBV capsid. The spectrum shows well-resolved charge states for charges in the  $140$ – $160 e$  range. The black line in Figure 5b shows the composite histogram obtained by binning the residual charge using  $0.01 e$  bins. The residual charge is the measured charge minus the integer charge (which is obtained by rounding the measured charge to the nearest integer). The blue line in Figure 5b shows the fit to the residual charge. The blue line was obtained by adding a Gaussian centered on a residual charge of  $0 e$  to the tails of identical Gaussians located at residual charges of  $-1.0 e$  and  $+1.0 e$  (as illustrated in Figure 1). The RMSD was then adjusted to give the best fit to the residual charge histogram. The RMSD that gives the best fit is  $0.221 e$ .

Figure 6a shows the charge histogram for the P22 procapsid generated using  $0.1 e$  bins. The spectrum shows resolved charge states for charges in the  $450$ – $500 e$  range; however, the charge states are not as well resolved as in the HBV histogram in Figure 5a. The black line in Figure 6b shows the composite histogram obtained by binning the residual charge using  $0.01 e$  bins. The blue line was obtained by fitting a Gaussian function (consisting of three overlapping Gaussians) to the residual

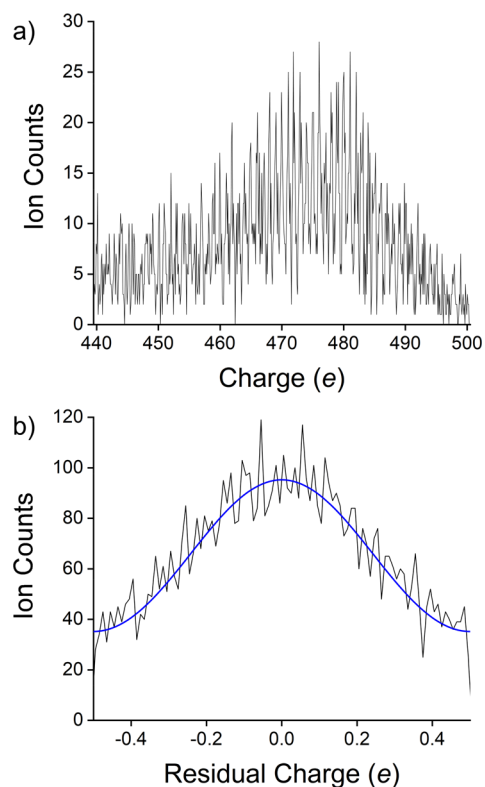


**Figure 6.** Charge-state resolution for the P22 procapsid. (a) The charge histogram generated using  $0.1 e$  bins. (b) Residual charge histogram plotted with a bin size of  $0.01 e$ . The residual charge is the measured charge minus the integer charge. The blue line was obtained by fitting a Gaussian function to the residual charge histogram. The Gaussian function was obtained by adding a Gaussian centered on a residual charge of  $0 e$  to the tails of identical Gaussians located at residual charges of  $-1.0 e$  and  $+1.0 e$ . The RMSDs of the component Gaussians were adjusted in unison to give the best fit to the histogram.

charge histogram, as described above for the HBV data. In this case the best fit was obtained with a RMSD of  $0.272 e$ .

**Charge Calibration Procedure and Linearity Test.** A charge-sensitive amplifier generates an output voltage inversely proportional to the integrated current at the input:

$$V = -\frac{1}{C_f} \int_0^t i(t) dt \quad (1)$$

The gain is inversely proportional to the feedback capacitance,  $C_f$ . In the amplifier used here, the feedback capacitor is provided by a small wire around 2 mm from the input JFET. The capacitance, around  $100 \text{ fF}$ , is too small to reliably measure (at least with the equipment available to us). Thus, the quantity that relates the FFT magnitude to the charge must be established by calibration with known charges.

Figure 7 shows a compilation of the charge spectra measured for pyruvate kinase (PK), HBV, bromo mosaic virus (BMV), and P22 procapsid that were used to calibrate the charge measurements. All the charge spectra show charge-state resolution. We start with an approximate value for the constant that relates the magnitude in the FFT to the measured charge and refine it through an iterative process. CDMS measurements were first performed for ubiquitin. The mass of ubiquitin is small ( $8.6 \text{ kDa}$ ), and the charge states are well separated in the  $m/z$  spectrum. The charge states can be

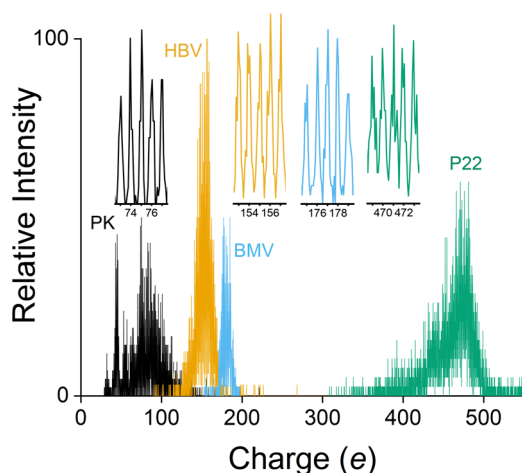


**Figure 7.** A composite histogram of the charge spectra used to calibrate the charge measurements. Results are shown for PK, HBV, BMV, and P22.

assigned using the known mass of ubiquitin and the measured  $m/z$  values. There is no ambiguity in the assignments. We used the 9–12 charge states. The ions were separated into the different charge states based on their  $m/z$  values, and then, the average measured charge associated with each integer charge state was calculated. The measured charges were plotted against the integer charge states, and a least-squares fit is used to determine the calibration constant,  $c$ , in the equation

$$q = c \times (q_m - q_n) \quad (2)$$

where  $q$  is the calibrated charge,  $q_m$  is the measured charge, and  $q_n$  is a small offset due to the noise in the FFT magnitude.  $q_n$  is set to zero at this point. Following this initial rough calibration, we move to larger species. For PK, the mass spectrum measured under native conditions contains features due to the tetramer and multimers of the tetramer. Using the calibration constant from ubiquitin, the initial charge states were assigned to the low-charge peaks for the PK tetramer, and then, the higher charge states for the tetramer and multimers were assigned by counting. The measured charge associated with each charge state was found by fitting a Gaussian to each peak in the charge spectrum. A least-squares fit to a plot of the measured charges against the assigned charge states provided a more refined value of  $c$ , and at this point, we also obtain a value for the offset  $q_n$ . PK mass distribution contains significant peaks due to the tetramer, octamer, dodecamer, and in some cases higher multimers. The charge assignments obtained above were tested by comparing the masses for the PK multimers determined by CDMS. With the correct charge assignments, the mass of the octamer is expected to equal twice the mass of the tetramer, and the mass of the dodecamer is expected to equal three times the mass of the tetramer. Adding one charge to the assigned values, or subtracting one charge, led to a situation where the masses of the multimers were no longer multiples of the tetramer mass. With the optimum charge assignments, we found that the masses of the octamer and dodecamer were very slightly larger than the expected masses, which we attributed to there being slightly more residual solvent or salt associated with the higher multimers.

After the PK charge states are assigned, it is straightforward to continue counting and to assign charge states to the peaks in the charge distributions measured for HBV and BMV. This

allowed us to go up to charges close to 200  $e$  (see Figure 7). At this point, a least-squares fit of the measured charges and assigned charge states for PK, HBV, and BMV provided more refined values of the calibration constant,  $c$ , and the offset  $q_n$ . It is evident from Figure 7 that there is a gap in the charge spectra from around 200  $e$  to around 440  $e$ , and then, the P22 ions have charges in the 440–500  $e$  range. We used the  $c$  and  $q_n$  values determined for ions with charges less than 200  $e$  to assign initial charge states to peaks resolved for P22. Measured charges were determined from a Gaussian and plotted against the assigned charge states. A least-squares fit of eq 1 to the P22 charge data was performed, keeping the value of  $q_n$  either fixed at the value for the smaller charges or set to zero. The assigned charge states for the P22 ions were adjusted to give the value of  $c$  that was closest to the value obtained for ions with charges of up to 200  $e$ . At this point, we combined the charge data for PK, HBV, BMV, and P22 and performed a least-squares fit to obtain final values for the calibration constant,  $c$ , and the offset,  $q_n$ . The result of the final calibration is shown in Figure 8a,

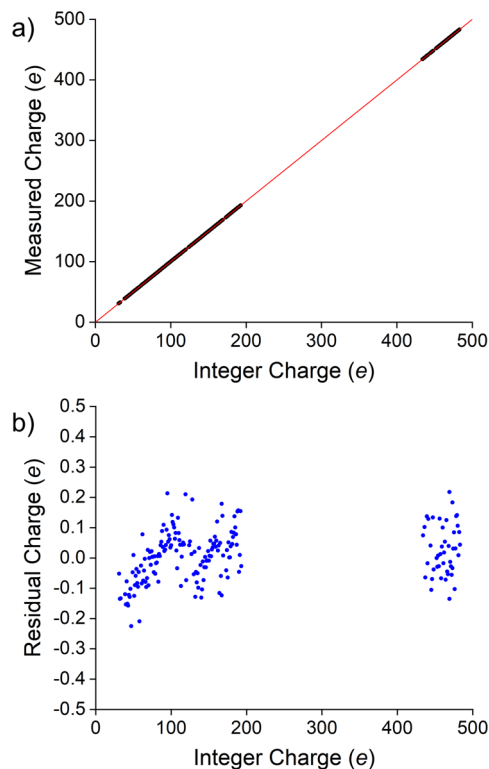


**Figure 8.** Charge calibration and linearity test. (a) Plot of the measured charge from Gaussian fits to the charge peaks against the integer charge. The black points are from the measurements, and the red line is a least-squares fit. (b) Plot of the residual charge (the measured charge from a Gaussian fit to the charge peaks minus the integer charge) against integer charge.

where the measured charge is plotted against the integer charge (the assigned charge state). The points show the data, and the red line is the fit. The  $r^2$  value (coefficient of determination) for the fit is 0.99999961. Figure 8b shows a plot of the residual charges (the measured charge minus the integer charge). Recall that the measured charges are determined from a Gaussian fit to the peaks in the charge spectrum. Thus, there is an uncertainty associated with the measured charges, which is proportional to the square root of the number of ions within each charge peak. Large values of

the residual charge in Figure 8b are usually associated with charge peaks with a small number of ions. However, even in cases where the number of ions in the charge peak is relatively small, the uncertainty is small enough that there is virtually no chance of assigning a peak to the wrong charge state.

The results presented above show that the charge calibration is linear over a range from a few charges up to 500 charges. Furthermore, the offset,  $q_m$ , is sufficiently small that it can be set to zero without a significant loss of accuracy. Thus, a single calibration constant is all that is required to accurately calibrate charges up to at least 500  $e$ . Having performed the calibration once, the use of dynamic calibration allows the charge calibration to be retained indefinitely or at least until modifications are made. When modifications are made to the CDMS instrument that might influence the calibration, we have found that it is not necessary to perform the full calibration outlined above. Exploiting the known response linearity, we have found that calibration with ubiquitin and HBV is sufficient.

## CONCLUSIONS

To measure the charge accurately enough that the charge state can be assigned with a high degree of confidence, the uncertainty in the charge measurement must be around 0.2  $e$  RMSD or better. We have shown that dynamic charge calibration enables the charge of an ion to be measured with a relative charge uncertainty of around  $5 \times 10^{-4}$ , enabling low-error charge-state assignment to be performed for ions carrying a charge of up to 500  $e$ . The mass-resolving power in CDMS is determined by the uncertainties in the charge and  $m/z$  measurements. When the charge state can be assigned to a high degree of certainty, the mass resolving power is determined by the  $m/z$ -resolving power, opening the door to high-resolving-power mass measurements for ions with masses in the tens of megadalton range.

## AUTHOR INFORMATION

### Corresponding Author

Martin F. Jarrold – Chemistry Department, Indiana University, Bloomington, Indiana 47405, United States; [orcid.org/0000-0001-7084-176X](https://orcid.org/0000-0001-7084-176X); Email: [mfj@indiana.edu](mailto:mfj@indiana.edu)

### Author

Aaron R. Todd – Chemistry Department, Indiana University, Bloomington, Indiana 47405, United States

Complete contact information is available at: <https://pubs.acs.org/10.1021/jasms.0c00081>

### Notes

The authors declare the following competing financial interest(s): A.R.T. declares no competing financial interest. M.F.J. is associated with a company that is developing charge detection mass spectrometry.

## ACKNOWLEDGMENTS

This material is based upon work supported by the National Science Foundation under Grant Number CHE-1531823. We would like to thank the IU Chemistry Department Electronic Instrument Services and Mechanical Instrument Services for their valuable contributions.

## REFERENCES

- (1) Shelton, H.; Hendricks, C. D.; Wuerker, R. F. Electrostatic acceleration of microparticles to hypervelocities. *J. Appl. Phys.* **1960**, *31*, 1243–1246.
- (2) Fuerstenau, S. D.; Benner, H. W. Molecular weight determination of megadalton DNA electrospray ions using charge detection time-of-flight mass spectrometry. *Rapid Commun. Mass Spectrom.* **1995**, *9*, 1528–1538.
- (3) Benner, W. H. A gated electrostatic ion trap to repetitiously measure the charge and  $m/z$  of large electrospray ions. *Anal. Chem.* **1997**, *69*, 4162–4168.
- (4) Maze, J. T.; Jones, T. C.; Jarrold, M. F. Negative droplets from positive electrospray. *J. Phys. Chem. A* **2006**, *110*, 12607–12612.
- (5) Mabbett, S. R.; Zilch, L. W.; Maze, J. T.; Smith, J. W.; Jarrold, M. F. Pulsed acceleration charge detection mass spectrometry: Application to weighing electrosprayed droplets. *Anal. Chem.* **2007**, *79*, 8431–8439.
- (6) Gamero-Castaño, M. Induction charge detector with multiple sensing stages. *Rev. Sci. Instrum.* **2007**, *78*, 043301.
- (7) Gamero-Castaño, M. Retarding potential and induction charge detectors in tandem for measuring the charge and mass of nanodroplets. *Rev. Sci. Instrum.* **2009**, *80*, 053301.
- (8) Smith, J. W.; Siegel, E. E.; Maze, J. T.; Jarrold, M. F. Image charge detection mass spectrometry: Pushing the envelope with sensitivity and accuracy. *Anal. Chem.* **2011**, *83*, 950–956.
- (9) Doussineau, T.; Yu Bao, C.; Clavier, C.; Dagany, X.; Kerleroux, M.; Antoine, R.; Dugourd, P. Infrared multiphoton dissociation tandem charge detection-mass spectrometry of single megadalton electrosprayed ions. *Rev. Sci. Instrum.* **2011**, *82*, 084104.
- (10) Doussineau, T.; Kerleroux, M.; Dagany, X.; Clavier, C.; Barbaire, M.; Maurelli, J.; Antoine, R.; Dugourd, P. Charging megadalton poly(ethylene oxide)s by electrospray ionization. A charge detection mass spectrometry study. *Rapid Commun. Mass Spectrom.* **2011**, *25*, 617–623.
- (11) Contino, N. C.; Jarrold, M. F. Charge detection mass spectrometry for single ions with a limit of detection of 30 charges. *Int. J. Mass Spectrom.* **2013**, *345–347*, 153–159.
- (12) Pierson, E. E.; Keifer, D. Z.; Selzer, L.; Lee, L. S.; Contino, N. C.; Wang, J. C.; Zlotnick, A.; Jarrold, M. F. Detection of late intermediates in virus capsid assembly by charge detection mass spectrometry. *J. Am. Chem. Soc.* **2014**, *136*, 3536–3541.
- (13) Pierson, E. E.; Contino, N. C.; Keifer, D. Z.; Jarrold, M. F. Charge detection mass spectrometry for single ions with an uncertainty in the charge measurement of 0.65  $e$ . *J. Am. Soc. Mass Spectrom.* **2015**, *26*, 1213–1220.
- (14) Doussineau, T.; Désert, A.; Lambert, O.; Taveau, J.-C.; Lansalot, M.; Dugourd, P.; Bourgeat-Lami, E.; Ravaine, S.; Duguet, E.; Antoine, R. Charge detection mass spectrometry for the characterization of mass and surface area of composite nanoparticles. *J. Phys. Chem. C* **2015**, *119*, 10844–10849.
- (15) Keifer, D. Z.; Motwani, T.; Teschke, C. M.; Jarrold, M. F. Measurement of the accurate mass of a 50 MDa infectious virus. *Rapid Commun. Mass Spectrom.* **2016**, *30*, 1957–62.
- (16) Pierson, E. E.; Keifer, D. Z.; Kukreja, A. A.; Wang, J. C.-Y.; Zlotnick, A.; Jarrold, M. F. Charge detection mass spectrometry identifies preferred non-icosahedral polymorphs in the self-assembly of woodchuck hepatitis virus capsids. *J. Mol. Biol.* **2016**, *428*, 292–300.
- (17) Keifer, D. Z.; Motwani, T.; Teschke, C. M.; Jarrold, M. F. Acquiring structural information on virus particles via charge detection mass spectrometry. *J. Am. Soc. Mass Spectrom.* **2016**, *27*, 1028–1036.
- (18) Pierson, E. E.; Keifer, D. Z.; Asokan, A.; Jarrold, M. F. Resolving adeno-associated viral particle diversity with charge detection mass spectrometry. *Anal. Chem.* **2016**, *88*, 6718–6725.
- (19) Delalande, L.; Tsvetkova, I. B.; Zeng, C.; Bond, K. M.; Jarrold, M. F.; Dagnea, B. Wrapping a virus in a molecular net. *Nanoscale* **2016**, *8*, 16221–16228.

- (20) Saxena, P.; He, L.; Malyutin, A.; Datta, S. A. K.; Rein, A.; Bond, K. M.; Jarrold, M. F.; Spilotros, A.; Svergun, D.; Douglas, T.; Dragnea, B. Virus matryoshka: Virus-like particles of immature HIV-1 assembled on bacteriophage-derived templates. *Small* **2016**, *12*, 5862–5872.
- (21) Doussineau, T.; Mathevon, C.; Altamura, L.; Vendrely, C.; Dugourd, P.; Forge, V.; Antoine, R. Mass determination of entire amyloid fibrils by using mass spectrometry. *Angew. Chem., Int. Ed.* **2016**, *55*, 2340–2344.
- (22) Elliott, A. G.; Harper, C. C.; Lin, H.-W.; Susa, A. C.; Xia, Z.; Williams, E. R. Simultaneous measurements of mass and collisional cross section of single ions with charge detection mass spectrometry. *Anal. Chem.* **2017**, *89*, 7701–7708.
- (23) Elliott, A. G.; Harper, C. C.; Lin, H.-W.; Williams, E. R. Mass, mobility and MS<sup>n</sup> measurements of single ions using charge detection mass spectrometry. *Analyst* **2017**, *142*, 2760–2769.
- (24) Motwani, T.; Lokareddy, R. K.; Dunbar, C. A.; Cortines, J. R.; Jarrold, M. F.; Cingolani, G.; Teschke, C. M. A viral scaffolding protein triggers portal ring oligomerization and incorporation during procapsid assembly. *Science Advances* **2017**, *3*, e1700423.
- (25) Lee, L. S.; Brunk, N.; Haywood, D. G.; Keifer, D.; Pierson, E.; Kondylis, P.; Wang, J. C.-Y.; Jacobson, S. C.; Jarrold, M. F.; Zlotnick, A. A molecular breadboard: Removal and replacement of subunits in a hepatitis B virus capsid. *Protein Sci.* **2017**, *26*, 2170–2180.
- (26) Lutomski, C. A.; Lykтей, N. A.; Pierson, E. E.; Zhao, Z.; Zlotnick, A.; Jarrold, M. F. Multiple pathways in capsid assembly. *J. Am. Chem. Soc.* **2018**, *140*, 5784–5790.
- (27) Dunbar, C. A.; Callaway, H. M.; Parrish, C. R.; Jarrold, M. F. Probing antibody binding to canine parvovirus with charge detection mass spectrometry. *J. Am. Chem. Soc.* **2018**, *140*, 15701–15711.
- (28) Kim, S. J.; Fernandez-Martinez, J.; Nudelman, I.; Shi, Y.; Zhang, W.; Raveh, B.; Herricks, T.; Slaughter, B. D.; Hogan, J.; Upla, P.; Chemmama, I. E.; Pellarin, R.; Echeverria, I.; Shivaraju, M.; Chaudhury, A. S.; Wang, J.; Williams, R.; Unruh, J. R.; Greenberg, C. H.; Jacobs, E. Y.; Yu, Z.; de la Cruz, M. J.; Mironska, R.; Stokes, D. L.; Aitchison, J. D.; Jarrold, M. F.; Gerton, J. L.; Ludtke, S. J.; Akey, C. W.; Chait, B. T.; Sali, A.; Rout, M. P. Structure and functional anatomy of the nuclear pore complex. *Nature* **2018**, *555*, 475–482.
- (29) Lutomski, C. A.; Gordon, S. M.; Remaley, A. T.; Jarrold, M. F. Resolution of lipoprotein subclasses by charge detection mass spectrometry. *Anal. Chem.* **2018**, *90*, 6353–6356.
- (30) Dunbar, C. A.; Rayaprolu, V.; Wang, J. C.-Y.; Brown, C. J.; Leishman, E.; Jones-Burrage, S.; Trinidad, J. C.; Bradshaw, H. B.; Clemmer, D. E.; Mukhopadhyay, S.; Jarrold, M. F. Dissecting the components of sindbis virus from arthropod and vertebrate hosts: Implications for infectivity differences. *ACS Infect. Dis.* **2019**, *5*, 892–902.
- (31) Shockley, W. Currents to conductors induced by a moving point charge. *J. Appl. Phys.* **1938**, *9*, 635–636.
- (32) Weinheimer, A. J. The charge induced on a conducting cylinder by a point charge and its application to the measurement of charge on precipitation. *J. Atmos. Oceanic Technol.* **1988**, *5*, 298–304.
- (33) Draper, B. E.; Jarrold, M. F. Real time analysis and signal optimization for charge detection mass spectrometry. *J. Am. Soc. Mass Spectrom.* **2019**, *30*, 898–904.
- (34) Hogan, J. A.; Jarrold, M. F. Optimized electrostatic linear ion trap for charge detection mass spectrometry. *J. Am. Soc. Mass Spectrom.* **2018**, *29*, 2086–2095.
- (35) Todd, A. R.; Alexander, A. W.; Jarrold, M. F. Implementation of a charge sensitive amplifier without a feedback resistor for charge detection mass spectrometry reduces noise and enables detection of individual ions carrying a single charge. *J. Am. Soc. Mass Spectrom.* **2020**, *31*, 146–154.
- (36) Draper, B. E.; Anthony, S. N.; Jarrold, M. F. The FUNPET- a new hybrid ion funnel-ion carpet atmospheric pressure interface for the simultaneous transmission of a broad mass range. *J. Am. Soc. Mass Spectrom.* **2018**, *29*, 2160–2172.
- (37) Bertuccio, G.; Rehak, P.; Xi, D. M. A novel charge sensitive preamplifier without the feedback resistor. *Nucl. Instrum. Methods Phys. Res., Sect. A* **1993**, *326*, 71–76.
- (38) Crowther, R. A.; Kiselev, N. A.; Böttcher, B.; Berriman, J. A.; Borisova, G. P.; Ose, V.; Pumpens, P. Three-dimensional structure of hepatitis B virus core particles determined by electron cryomicroscopy. *Cell* **1994**, *77*, 943–950.
- (39) Wynne, S. A.; Crowther, R. A.; Leslie, A. G. W. The crystal structure of the human hepatitis B virus capsid. *Mol. Cell* **1999**, *3*, 771–780.